

---

**1 Profiles of Wind Veer and Wind Speed in Turbulent  
2 Ekman Flow**

**3 Cedrick Ansorge, Hauke Wurps**

**4**  
**5** Draft - Version July 9, 2024

**6 Abstract**

**7** The profiles of wind speed and direction in turbulent Ekman flow are formulated  
**8** based on asymptotic theory and data from direct numerical simulation. The profile  
**9** of the streamwise component follows the classical viscous, logarithmic and wake  
**10** scaling. In the outer layer, the velocity component profiles can be described by an  
**11** Ekman-spiral with adapted boundary conditions that result in a reduction of the  
**12** spiral-like rotation. The span-wise component poses a conceptual challenge to the  
**13** channel-flow analogy in the context of asymptotic matching; it exhibits a mixed  
**14** scaling in the surface layer, but follows outer scaling for most of the outer layer.  
**15** Viscous stress scales universally across the boundary layer in inner units while  
**16** the total stress becomes universal as a function of outer height. This implies a  
**17** mixed scaling for the turbulent stress and eddy viscosity across the inner layer  
**18** and convergence to a universal scaling as function of the outer height across the  
**19** outer layer for increasing scale separation vide Reynolds numbers.

**20 1 Introduction**

**21** The Coriolis force bends the path of motion on a rotating sphere and establishes  
**22** geostrophic equilibrium when in balance with a pressure gradient force. Wind veer  
**23** away from the wind direction in geostrophic equilibrium is (i) due to direct fric-  
**24** tional effects in the very vicinity of the surface and (ii) due to turbulence which  
**25** exerts indirect frictional effects; these effects cause a slow-down of the mean wind  
**26** reducing the Coriolis force thus turning the wind in favor of the pressure gradient  
**27** force. Not only does the veering set the frame of reference for surface layer theory,  
**28** it also has effects at small and large scales from large-scale dispersion via plume  
**29** spreading to cyclone spin-down (Svensson and Holtlag 2009) and on the capa-  
**30** bilities of data assimilation and accuracy of surface flux estimates (Brown et al.  
**31** 2005). From a large-scale perspective, the veering of wind across the planetary  
**32** boundary layer determines the amount of cross-isobaric mass-flux, commonly re-  
**33** ferred to as 'Ekman pumping' (Ekman 1905), and it is thus a key factor in the

---

Address(es) of author(s) should be given

34 life-cycle of large-scale synoptic systems. Within the atmospheric boundary layer  
 35 (ABL), directional shear of the wind in the upper part of the surface layer may  
 36 cause a systematic yaw for tall wind power generation devices where blades reach  
 37 into the Ekman layer, i.e. that part of the boundary layer where the wind starts to  
 38 turn; an exact estimate of such effects is critical in the site assessments for wind  
 39 farms (Calaf et al. 2010; Mirocha et al. 2018).

40 In the planetary boundary layer, wind veer is characterized by the surface  
 41 veering angle  $\alpha$  defined as the angle between the negative surface shear stress  
 42  $\tau_{\text{sfc}}$  and the geostrophic wind. Surface veering  $\alpha$  and geostrophic drag  $Z \equiv u_{\star}/G$ ,  
 43 where the friction velocity  $u_{\star} \equiv \sqrt{|\tau_{\text{sfc}}|/\rho}$ , uniquely determine the surface drag  $\tau_{\text{sfc}}$   
 44 in a turbulent Ekman flow. In any quantitative description of the surface layer, the  
 45 friction velocity  $u_{\star}$  is the dynamic scale and  $\alpha$  defines the alignment of the frame  
 46 of reference. Knowledge about  $u_{\star}$  and  $\alpha$  is thus a prerequisite for any quantitative  
 47 theory of the surface layer, and Rossby and Montgomery (1935) constrained the  
 48 two parameters based on integral relations in the ABL. Asymptotic similarity  
 49 theory was later used by Tennekes (1973); Blackadar and Tennekes (1968), and—  
 50 based on his seminal direct numerical simulations (DNS) of Ekman flow—, Spalart  
 51 (1989) suggested a modification to take into account effects of low to intermediate  
 52 Reynolds numbers. Later on, constants were re-evaluated with a focus on the ABL  
 53 based on observations (Högström 1988, 1996) and numerical modelling (Spalart  
 54 et al. 2008, 2009; Ansorge and Mellado 2014; Ansorge 2019).

55 Attempts were also undertaken to obtain profiles of the wind speed: One ap-  
 56 proach is to match the inner and outer layer at a reference height; Etling (2002);  
 57 Emeis (2018) (Sec. 21.10; Eq. 21.48) choose the Prandtl-layer height  $z_{\text{Prandtl}}$  to  
 58 match the wind speed profiles, which, however, requires external prescription of  
 59  $\alpha(z_{\text{prandtl}})$ , the veering at that height. A one-dimensional profile with constant  
 60 veering is given by Emeis et al. (2007, Sec. 3; Eq. 3.1-3.19).

61 Gryning et al. (2007) present an extension of the wind-speed profile beyond the  
 62 surface layer using a neutral reference profile and a stability correction; Kelly and  
 63 Gryning (2010), based on a probabilistic representation of stratification, develop  
 64 a model for the long-term mean wind speed in the ABL and compare this with  
 65 observation at different sites; Kelly and Troen (2016) demonstrate the effect of  
 66 such improved model for wind-energy applications. In consideration of the large  
 67 scale separation in geophysical flow, the rotation of the wind in the surface layer is  
 68 often assumed negligible, and above investigations merely focus on the wind speed;  
 69 that means, the veering of the wind with height is not described and there is little  
 70 knowledge on the profile of the span-wise velocity component and the precise  
 71 shape of the hodograph in the limit of a truly neutral Ekman boundary layer. A  
 72 climatology of wind turning in the ABL is given by Lindvall and Svensson (2019)  
 73 Klein et al. (2021) use a statistical turbulence modelling approach that yields a  
 74 two-component velocity profile, but they also find that the exact representation of  
 75 turning is challenging.

76 Ekman-layer models are roughly based on Ekman's seminal 1905 paper in  
 77 combinations with additional assumptions, such as a prescribed profile shape for  
 78 eddy viscosity Ellison (1955) and two-layer models of the ABL take into account  
 79 rotational effects at higher altitudes, for instance when the wind speed needs to  
 80 be evaluated at heights on the order of 100 – 200 m, a particular concern when  
 81 it comes to wind-power forecasting (Optis et al. 2014). Despite rotational effects  
 82 being considered, the formulation of these models for the outer layer and analysis

83 of their performance primarily focuses on wind speed. Still, in 2018, Jiang et al.  
 84 recognized that the outer part of the Ekman boundary layer receives less attention  
 85 in comparison with the surface layer and study the neutral problem by Large-Eddy  
 86 simulation (LES). They focus on the wind speed and find an extended logarithmic  
 87 layer when considering the wind speed instead of the shear-aligned component, and  
 88 they eventually demonstrate by means of an analytical model that this vertical  
 89 extension of the logarithmic layer may be explained by a transfer of stress to the  
 90 span-wise velocity component where it is assumed that the shear vector  $\tau(z)$  and  
 91 stress vectors  $(\partial_z U, \partial_z V)$  are aligned.

92 More recently, Ghannam and Bou-Zeid (2021) treated the horizontally av-  
 93 eraged momentum budget to show that departures from shear-alignment in the  
 94 vicinity of the surface result in an integral of the wind veer ( $\alpha_M$  in their notation)  
 95 over the height to very high accuracy ( $\int_{z_0}^H \sin \alpha_M$  in their notation; their Eq. (16)).  
 96 Classic surface-layer similarity is recovered when the angle  $\alpha_M$  does not depend  
 97 on height, i.e., the wind veer is constant across the surface layer. If, however, the  
 98 wind veer depends on height, the profiles of stress and mean velocities depart from  
 99 the scalings implied by classic surface-layer similarity.

100 Turbulent Ekman flow is considered here as a conceptual model of the homo-  
 101 geneous, stationary ABL over a flat surface under neutral stratification. Universal  
 102 profiles of the wind vector for turbulent Ekman flow not only are a well-described  
 103 limit for theoretical exploration or higher-order approaches taking into account  
 104 possible effects of stratification, roughness or other physical complications encoun-  
 105 tered in the real geophysical system. While, on first sight, the study of such a  
 106 strongly idealized case appears as an academic problem, it contains the essence  
 107 of surface similarity as it is used in most atmospheric models, be it conceptual  
 108 or numeric ones. More complex accounts generally refer to the homogeneous sta-  
 109 tionary problem as a base state: (i) Roughness is commonly incorporated by a  
 110 linear transformation of vertical scale involving the roughness parameter  $z_0$  and  
 111 for larger roughness also a displacement height (Monin and Yaglom 1975; Jacobs  
 112 and Van Boxel 1988; Högström 1988); (ii) Stability can be accounted for by a  
 113 linearization around the neutrally stratified profile (Monin 1970; Monin and Ya-  
 114 glom 1975; Högström 1988, 1996; Sakagami et al. 2020); (iii) Non-stationarity in  
 115 the pressure-gradient forcing can be accounted for by a linear damped-oscillator  
 116 approach around the base state (Momen and Bou-Zeid 2016); (iv) Barotropic and  
 117 baroclinic effects on the velocity profile require to consider the height-dependence  
 118 of the veer and stress misalignment (Momen et al. 2018; Ghannam and Bou-Zeid  
 119 2021). Furthermore, such a solution can serve as better initial condition for numer-  
 120 ical simulation of the flow, to minimize the length of initial transient periods, or  
 121 as benchmark for turbulence closures that can be tuned to reproduce the neutral  
 122 limit case.

123 Despite the strong simplifications implied by our choice of set-up, there is no  
 124 straightforward approach to solving this well-defined problem. Large-Eddy simula-  
 125 tion not only needs to be tuned for the surface shear stress and veering angle, but  
 126 it also relies on sub-grid closures that commonly assume alignment of the turbu-  
 127 lent stress with gradients. This pre-requisite is not fulfilled when the wind rotates  
 128 with height. Esau (2004) investigated the representation of the Ekman boundary  
 129 layer by dynamical subgrid closures and Zikanov et al. (2003) proposed a closure  
 130 for the wind profile using a linearized representation of the eddy viscosity. Despite  
 131 advances in analysis of this simplified set-up (Jiang et al. 2018), there is yet insuf-

132 ficient understanding for a quantitative generalization of the results to arbitrary  
 133 external forcing (manifest in variation of the Reynolds number) – and indeed the  
 134 fundamental questions pertaining to such relatively simple dynamics of turbulence  
 135 are not reflected in the research on LES for the ABL over the past 50 years (Stoll  
 136 et al. 2020).

137 At the same time, an increasing amount of high-quality and high-resolution  
 138 data from turbulence-resolving approaches is emerging due to recent advances in  
 139 high-performance computing and its application to geophysical problem sets; the  
 140 geophysical range of scale separation, however, is—and it will remain so for the  
 141 foreseeable future—out of reach for such simulation (Dimotakis 2005). Here, the  
 142 routinely employed concept of Reynolds-number similarity can help. It postulates  
 143 the existence of *fully developed turbulence* believed to occur for a sufficiently large  
 144 but finite Reynolds number (Barenblatt and Goldenfeld 1995). (Already in 1998,  
 145 this in fact lead Moin and Mahesh to the question *how high a Re is high enough?*)  
 146 Certain statistics of fully developed turbulence, such as dissipation (Dimotakis  
 147 2005) or profiles of mean velocity (Barenblatt 1993), become independent of the  
 148 Reynolds number when appropriately scaled; other statistics, such as the near-  
 149 wall maximum in velocity fluctuation depend on Re (Baars and Marusic 2020)  
 150 and externality of the flow may exert an impact on near-wall scaling (da Silva  
 151 et al. 2014). It appears that for certain statistics in Ekman flow, fully-developed  
 152 turbulence is reached with the Reynolds numbers that became possible due to an  
 153 increase of computing capabilities over the past decades.

154 This paper exploits the robust features of mean velocity profiles from direct  
 155 numerical simulation across a range of Reynolds numbers to formulate both the  
 156 streamwise and span-wise components of the mean velocity vector as a function  
 157 of the Reynolds number.

## 158 2 Problem Formulation and Numerical Approach

159 We consider here incompressible, turbulent Ekman flow, that is, the turbulent flow  
 160 over a flat rotating plate, as a physical model for the truly neutral ABL. The f-  
 161 plane approximation is applied such that rotation only acts on horizontal velocity  
 162 components; we thus neglect rotational effects on the horizontal components of  
 163 velocity and dynamical effects due to latitudinal variation of the rate of rotation.

### 164 2.1 Notation and Governing Equations

165 The dimensional velocity vector of the numerical simulations is  $\underline{U} = (U_1, U_2, U_3) =$   
 166  $(U, V, W)$  over the coordinate system  $Oxyz$ , where an approximate alignment  
 167 (plus/ minus few degrees) of the direction  $Ox$  with the surface shear stress is  
 168 achieved. The coordinate  $Oz$  points away from the wall, and  $Oy$  points in the  
 169 span-wise direction normal to  $Oxz$ . For analysis of the results, we use two coordi-  
 170 nate systems that are (i) exactly aligned with the surface shear stress

$$\tau_{\text{sfc}} = \begin{pmatrix} \tau_x \\ \tau_y \\ \tau_z \end{pmatrix} = -\nu \left( \frac{\partial U}{\partial z} \hat{e}_x + \frac{\partial V}{\partial z} \hat{e}_y \right) \quad (1a)$$

and labelled by an upper index  $\alpha$  as in  $\underline{U}^\alpha$  for the velocity vector, and (ii) the coordinate system aligned with the free-atmosphere geostrophic wind labelled by an upper index  $G$  as in  $\underline{U}^G$ . We denote the modulus of the surface shear, the surface friction, by

$$u_* = \sqrt{\|\tau_{\text{sfc}}\|} \quad (1b)$$

and let  $Z_* = G/u_*$ ; the surface veering angle  $\alpha_*$  is the angle between  $\tau$  and the geostrophic wind

$$\alpha_* = \sphericalangle(\underline{G}, \underline{\tau}_{\text{sfc}}). \quad (1c)$$

Analogously, we denote the height-local veering of the wind  $\alpha(z) = \sphericalangle(\underline{G}, \underline{U}(z))$ , where  $\underline{G} = (G_1, G_2, 0)$  is the geostrophic wind vector.

We consider the incompressible Navier–Stokes equations for the three velocity components on the f-plane in a framework that is governed by (i) geostrophic wind magnitude  $G = \sqrt{G_1^2 + G_2^2}$ , (ii) Coriolis parameter  $f$  (representing the angular rotation), and (iii) kinematic viscosity  $\nu$ . In absence of external variability, this system converges to a statistically steady state in the sense that flow statistics do not depend on time; and this state is defined by a Reynolds number, the only non-dimensional parameter that governs the system. We use the geostrophic wind as velocity and the Coriolis parameter  $f$  as time scale for the non-dimensional framework. This implies the Rossby radius  $A_{\text{Ro}} = G/f$  as length scale, such that one Reynolds number governing the problem reads as

$$\text{Re}_A = \frac{GA_{\text{Ro}}}{\nu}. \quad (2)$$

The scales used in defining  $\text{Re}_A$  are of limited relevance for description of the turbulent flow state. The turbulence scale separation in a wall-bounded flow is commonly characterized by the friction Reynolds number (?):

$$\text{Re}_\tau = \frac{u_* \delta}{\nu} = \delta^+ = \frac{\text{Re}_A}{Z_*^2}, \quad (3)$$

where  $\delta = u_*/f$  and we use a superscript '+' to denote normalization by inner turbulence scales  $(u_*, \nu)$ . Another common measure of scale separation is the Reynolds number defined by the laminar Ekman layer thickness  $D = \sqrt{2\nu/f}$ ,

$$\text{Re}_D = \frac{GD}{\nu} = \sqrt{2\text{Re}_A}. \quad (4)$$

Another common measure of scale separation is the Reynolds number defined by the laminar Ekman layer thickness  $D = \sqrt{2\nu/f}$ ,

$$\text{Re}_D = \frac{GD}{\nu} = \sqrt{2\text{Re}_A}. \quad (5)$$

The governing equations non-dimensionalized by  $G$ ,  $f$ , and  $A_{\text{Ro}}$  read as

$$\frac{\partial u_i}{\partial t} = \frac{\partial \pi}{\partial x_i} - u_j \frac{\partial u_i}{\partial x_j} + \epsilon_{i2j} (u_j - G_j) + \frac{1}{\text{Re}} \frac{\partial^2 u_i}{\partial x_j^2} \quad (6a)$$

$$\frac{\partial u_j}{\partial x_j} = 0, \quad (6b)$$

Table 1: Direct numerical simulation data sets used in this work.  $Re_A$  and  $Re_D$  refer to the Reynolds number defined in terms of the Rossby radius  $\Lambda$  and Ekman-layer thickness  $D$  respectively.  $L_{xy}$  is the domain size in the stream- and span-wise direction. The grid is given by the number of grid points in the stream-wise ( $N_x$ ), span-wise ( $N_y$ ) and vertical ( $N_z$ ) directions respectively. The resolution in the span-wise and stream-wise directions are given as  $\Delta x^+$  and  $\Delta y^+$ . The grid in the vertical is stretched, and resolution at the wall is given by  $\Delta z^+$ .

$Re_A$	$Re_D$	$L_{xy}/\Lambda$	$N_x \times N_y \times N_z$	$\Delta x^+$	$\Delta y^+$	$\Delta z^+ _{z=0}$
125 000	500	1.08	$2048 \times 2048 \times 192$	4.1	4.1	1.05
281 250	750	1.08	$3072 \times 3072 \times 384$	5.6	5.6	1.60
500 000	1 000	1.08	$3072 \times 6144 \times 512$	9.3	4.7	1.14
845 000	1 300	0.54	$2560 \times 5120 \times 640$	8.9	4.5	0.99
1 280 000	1 600	0.54	$3860 \times 7680 \times 960$	8.6	4.3	1.00

Table 2: DOIs and reference to the openly accesible data set at refubium repository

$Re_D$	DOI	Reference
500	<a href="https://doi.org/10.17169/refubium-42505">10.17169/refubium-42505</a>	Ansorge (2024a)
1000	<a href="https://doi.org/10.17169/refubium-42507">10.17169/refubium-42507</a>	Ansorge (2024b)
1300	<a href="https://doi.org/10.17169/refubium-42508">10.17169/refubium-42508</a>	Ansorge (2024c)
1600	<a href="https://doi.org/10.17169/refubium-42509">10.17169/refubium-42509</a>	Ansorge (2024d)

198 where  $u_i = U_i/G$  are the non-dimensional components velocity,  $\pi$  is non-dimensional  
 199 pressure,  $g_j = G_j/G$  are non-dimensionalized components geostrophic wind (with  
 200  $g_1^2 + g_2^2 = 1$  by construction), and  $\epsilon$  is the Levi–Civita tensor. These equations are  
 201 solved inside a bounded cube of size  $L_x \times L_y \times L_z$  with periodic boundary condi-  
 202 tions in the lateral (streamwise and spanwise) directions, a no-slip–no-penetration  
 203 boundary at  $z = 0$ , and a no-penetration, free-slip boundary at  $z = L_z$ .

## 204 2.2 Numerical Simulations

205 The problem is solved numerically by tLab<sup>1</sup>, an open-source tool-suite to simulate  
 206 and analyze turbulent flows. We use here a fourth-order–five-step Runge–Kutta  
 207 integration and sixth-order compact schemes for spatial derivatives in all direc-  
 208 tions. The incompressibility constraint is enforced by a fractional step approach  
 209 where the Poisson equation for the pressure field is solved to machine accuracy  
 210 using a combined spectral/compact approach as described in Mellado and Ansorge  
 211 (2012).

212 Simulations used here are shown in Tab. 1. We extend an existing set of simula-  
 213 tions for  $Re_A \in \{125\,000; 281\,250; 500\,000\}$  (gray shading; cf. Ansorge and Mellado  
 214 2014, 2016) by new simulations at higher Reynolds numbers up to  $Re_A = 1.28 \times 10^6$   
 215 with a horizontal domain extent up to  $3.3 \times 10^4$  viscous units. In total, this yields  
 216 one order of magnitude variation in terms of the scale separation in the boundary  
 217 layer.

<sup>1</sup> <https://github.com/turbulencia/tlab>

---

**218 3 Scaling behavior of the flow for  $Re_\tau$  up to 3000**

219 The generalization of profiles to arbitrary Reynolds numbers requires sufficient  
 220 scale separation in the simulations, not only to quantify the effect of the Reynolds  
 221 number on low-order flow statistics, but also to assess the corresponding rate-of-  
 222 change to eventually allow for an extrapolation of the findings. While the simula-  
 223 tions previously available (gray shading in Tab. 1) give confidence in a first-order  
 224 representation of the turbulent problem, the estimation of higher-order effects  
 225 such as the dependency of the Reynolds number requires a broader scale sepa-  
 226 ration that is made available by the two new simulations at increased Reynolds  
 227 number (cf. Tab. 1). Data at such scale separation has been obtained previously  
 228 (cf. Spalart et al. 2008, 2009), but we also need high confidence with respect to  
 229 the convergence of simulation data for slow oscillations and with respect to sam-  
 230 pling convergence, which translates to two further requirements on the data: First,  
 231 data should be free of artifacts from long-term oscillations across the vertical ex-  
 232 tent of the domain—primarily, simulations should be free of effects originating from  
 233 the inertial oscillation; this is achieved here by replacing the mean value of the  
 234 three-dimensional velocity fields by the time mean over a whole inertial oscilla-  
 235 tion. Second, high accuracy is also needed in terms of the statistical convergence  
 236 of averages, bulk measures and large-scale structures; this requires a domain size  
 237  $L_x > \mathcal{O}(\delta_{95})$ . We use here  $L_x = L_y = 1.08\Lambda$  for cases with  $Re \leq 1000$  and  
 238  $L_x = L_y = 0.54\Lambda$  for  $Re \geq 1300$  which corresponds to  $L_x/\delta_{95} \approx 25$  for  $Re_D = 500$   
 239 and  $L_x/\delta_{95} \approx 18$  for  $Re_D = 1300$ .

240 Bulk parameters of the simulations are given in Tab. 3. The surface stress is  
 241 characterized by  $u_*$  and  $\alpha_*$  in relation to the geostrophic wind vector and discussed  
 242 in more detail as the drag law below in Sec. 4.1 (we find the expected slight  
 243 decrease of  $u_*$  and  $\alpha_*$  with increasing  $Re$ ). The boundary-layer height estimated  
 244 from the 95% stress reduction,  $\delta_{95}$ , is around  $0.6\delta$  to  $0.66\delta$ . Interestingly, the  
 245 integrated TKE  $\int_0^\delta edz$  stays constant when normalized by the friction velocity  $u_*$   
 246 while the integrated dissipation  $\int_0^\delta \epsilon dz$  exhibits inviscid scaling when normalized  
 247 by the magnitude  $G$  of the geostrophic wind. (TKE and dissipation normalized as  
 248  $fG^{-3} \int edz$  and  $u_*^{-3} \int \epsilon dz$ , exhibit substantial dependence on  $Re$  for the variation  
 249 of  $u_*$ .) This indicates that the bulk dissipation is governed by the forcing  $G$ —  
 250 irrespective of  $Re$ . Changes in  $Re$ , however, affect the level and organization of  
 251 turbulence, and the parameter representing this dependency is the friction velocity  
 252  $u_*$  which describes the turbulence production processes in the surface layer, in  
 253 particular in the buffer layer.

254 Velocity profiles in inner units ( $U^+(z^+)$ , Fig. 1a) and outer units ( $U^-(z^-)$ ,  
 255 Fig. 1b) are in accordance with previous work (Coleman et al. 1992; Spalart et al.  
 256 2008, 2009; Ansorge and Mellado 2014; Ansorge 2019): The profiles of the shear-  
 257 aligned streamwise velocity component are well-collapsed for  $Re_D > 500$  below  
 258  $z^- \approx 0.15$  (circles in Fig. 1a); the case with  $Re_D = 500$  is only transitionally  
 259 turbulent and there is no distinct inner-outer scale separation. The logarithmic  
 260 law is appropriate for  $50 < z^+ < 0.15Re_\tau$ , where  $z^+ = Re_\tau z^-$ . While the profiles  
 261  $U^{\alpha*+}(z^+)$  diverge between different  $Re$  beyond  $z^- = 0.15$ , the corresponding  
 262 profiles of the velocity deficit ( $U^{\alpha*}(z^-) - G_1^\alpha$ )/ $u_*$  agree closely, irrespective of  $Re$ .  
 263 This illustrates the inner–outer scale-duality in this external flow with inner scaling  
 264 being appropriate in the inner layer and outer scaling in the outer layer. Also in

Table 3: Bulk characterization of the simulations for different Reynolds numbers  
 Viscous Reynolds number  $\text{Re}$ , friction Reynolds number  $\text{Re}_\tau$ , friction velocity  $u_*$ ,  
 surface veering angle  $\alpha_*$ , normalized boundary layer depth  $\delta_{95}/\delta$ , inner normalization  
 of vertically integrated TKE, outer normalization of vertically integrated dissipation.

$\text{Re}$	$\delta^+ = \text{Re}_\tau$	$u_*$	$\alpha_*$	$\delta_{95}/\delta$	$f u_*^{-3} \int_0^\delta \epsilon dz$	$G^{-3} \int_0^\delta \epsilon dz$
500	479	0.0619	25.5	0.66	0.88	1.31
750	886	0.0561	21.0	0.65	0.90	1.34
1000	1403	0.0530	18.8	0.62	0.92	1.30
1300	2122	0.0501	17.9	0.59	0.85	1.24
1600	2978	0.0482	17.2	0.61	0.91	1.21

265 the outer layer of the flow,  $u_*$  (and not the magnitude of the geostrophic wind  
 266  $G$ ) governs the inviscid normalization, i.e. a scaling independent of the Reynolds-  
 267 number.

268 No collapse in inner units is found for the profiles of spanwise velocity  $V^{\alpha*+}(z^+)$ .  
 269 When normalized in outer units, the deficit profiles of spanwise velocity  $(V^{\alpha*}(z^-) -$   
 270  $G_2^\alpha)/u_*$  agree well beyond  $z^- \approx 0.3$ . This is a much higher level in comparison  
 271 with the streamwise component that collapses also within the overlap layer, i.e.  
 272 much closer to the surface (circles in Fig. 1b). The value of  $V^{\alpha*+}(z^-) - G_2^\alpha$  is sen-  
 273 sitive to the wind veering for  $z \rightarrow 0$  as—for use of the shear-aligned component—it  
 274 has to approach the value  $-G_2^\alpha = |G| \sin \alpha \neq 0$  in view of the no-slip boundary  
 275 condition. While low-Re effects appear to be present for  $\mathcal{O}(\text{Re}) < 10^3$ , the span-  
 276 wise component converges to an Re-independent limit within the range of scale  
 277 separation considered here, i.e.

$$G_2^\alpha/u_* = Z_* \sin \alpha \rightarrow \text{const. for } \text{Re} \rightarrow \infty, \quad (7)$$

278 which has indeed already been found by Spalart (1989), who estimates the constant  
 279 from an integral relation.

280 The viscous stress

$$S_{\text{visc}} = \nu \sqrt{\left( \frac{\partial U}{\partial z} \right)^2 + \left( \frac{\partial V}{\partial z} \right)^2} \quad (8a)$$

281 exhibits universal scaling when considered as  $S_{\text{visc}}^+(z^+)$  (Fig. 2a); this normaliza-  
 282 tion is also appropriate in the outer layer where the viscous stress is, however,  
 283 small. Small deviations from the universal profile are observed for the smallest  
 284 Reynolds number  $\text{Re} = 500$ ; we attribute these to low-Re effects in the only tran-  
 285 sitionally turbulent flow ( $\text{Re}_\tau = 479$ ). In contrast to the viscous stress, the total  
 286 stress follows outer normalization, i.e.  $S^+(z^-)$  is universal; a discrepancy in the  
 287 inner layer does not occur as the total stress is approximately constant in the  
 288 viscous and buffer layer, and a rescaling of the height would have no effect there;  
 289 above, outer scaling is appropriate for the well-established dynamics in the over-  
 290 lap region of inner and outer layer. This, however, implies a mixed scaling for the  
 291 turbulent stress,

$$S_{\text{turb}} = \sqrt{\overline{uw}^2 + \overline{vw}^2}. \quad (8b)$$

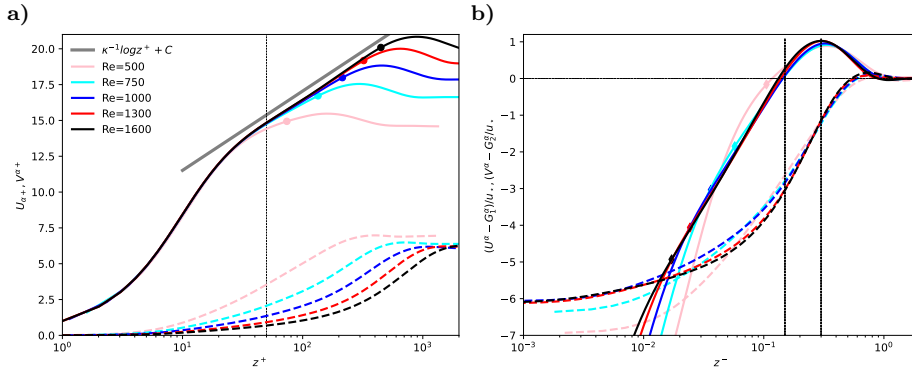


Fig. 1: **a)** Shear-aligned velocity profiles in inner units; **b)** Shear-aligned velocity deficit in outer units; circles mark the height  $z^- = 0.15$ ; dashed line gives the best logarithmic fit to the data.

Indeed,  $S_{\text{turb}}$  only follows inner normalization below  $z^+ \lesssim 20$  (where the turbulent contribution is negligible). In the outer layer, where  $S_{\text{visc}} \rightarrow 0$ ,  $S_{\text{turb}}^+$  follows outer normalization for  $z^- \gtrsim 0.15$ —with increasing accuracy for larger  $\text{Re}$  and larger distance from the surface. In the overlap region, i.e. for  $z^+ > 20$  and  $z^- < 0.15$ , the mixed scaling for the turbulent stress can be expressed as

$$S_{\text{turb}}^+(z^+, \text{Re}_\tau) = S^+(z^-) - S_{\text{visc}}^+(z^+), \quad (8c)$$

where  $z^- = z^+/\text{Re}_\tau$ .

The Eddy viscosity plays a crucial part when modelling profiles and the vertical transport in turbulent flow. In analogy to the Fick-law for molecular diffusion, the eddy diffusivity is the effective diffusivity that yields the turbulent transport  $S_{\text{turb}}$  based on the strain rate. For the symmetries in the flow (horizontal homogeneity, and  $W = 0$ ), it is

$$\nu_E = \frac{S_{\text{turb}}}{\sqrt{\left(\frac{\partial U}{\partial z}\right)^2 + \left(\frac{\partial V}{\partial z}\right)^2}} = \nu \frac{S_{\text{turb}}}{S_{\text{visc}}}. \quad (9a)$$

The inner normalization of  $\nu_E$  is obtained when dividing by the molecular viscosity:

$$\nu_E^+ = \nu_E / \nu = S_{\text{turb}} / S_{\text{visc}}. \quad (9b)$$

Under this normalization, the profiles of eddy viscosity collapse below  $z^+ \approx 20$  with a tendency towards better collapse at higher  $z^+$  for higher Reynolds number (up to  $z^+ \approx 50$  for  $\text{Re} = 1600$ ; Fig. 2c). In the outer layer, the eddy viscosity is characterized by a distinct minimum at  $z^- \approx 0.6 - 0.8$ , and we find that the following mixed normalization of  $\nu_E$  by the geostrophic wind and friction velocity collapses the value of  $\nu_E$  at this minimum (cf. Fig. 2d):

$$\nu_E^- = \nu_E^+ \frac{1}{\delta^+} = \nu_E \frac{1}{\nu} \frac{\nu}{u_* \delta} = \nu_E \frac{f}{u_*^2}. \quad (9c)$$

Substantial variation of the profiles is, however observed below and above this minimum for different  $\text{Re}$  which illustrates that this normalization is probably not generally appropriate across the outer layer.

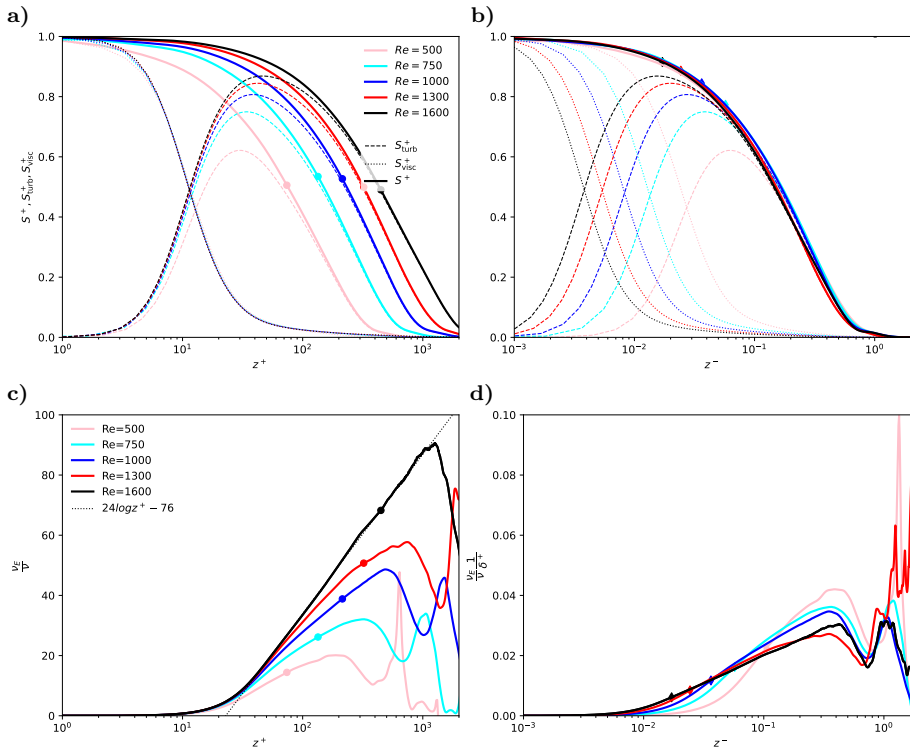


Fig. 2: **a-b)** Profiles of the turbulent stress  $S_{\text{turb}}^+$  (dashed), the viscous stress  $S_{\text{visc}}^+$  (dotted), and the total stress,  $S^+ = S_{\text{visc}}^+ + S_{\text{turb}}^+$  (solid) as a function of inner height **(a)** and outer height **(b)**. **c-d)** Normalized eddy viscosity  $\nu_E$  (solid) plotted versus inner **(c)** and outer height **(d)**. Different colors are for different Reynolds numbers (cf. Tab. 1). Circles in **(a)** and **(c)** denote the height  $z^- = 0.15$ , diamonds in **(b)** and **(d)** are for  $z^+ = 50$  as in Fig. 1.

313 The organization of the flow is depicted in terms of the turbulence kinetic en-  
 314 ergy in Fig. 3. In vicinity of the wall, at  $y^+ \approx 10$ , (Fig. 3a), elongated streaks  
 315 aligned with the surface shear stress dominate. Moving away from the wall, to  
 316  $y^+ \approx 150$  (well within the logarithmic region), the structures are larger and more  
 317 isotropic, but they are still largely aligned with the surface shear stress. In the  
 318 upper part of the outer layer, around  $y^+ \approx 1000$ , no clear signature of the sur-  
 319 face veering direction is found, and intense TKE structures (bright yellow) are  
 320 organized on a large spatial scale with weaker eddies (greenish structures) and  
 321 quiescent regions in between.

#### 322 4 A universal velocity profile for the turbulent Ekman layer

323 We now turn to the formulation of a general velocity profile that is fully determined  
 324 by the only parameter of the idealized problem, namely a Reynolds number repre-

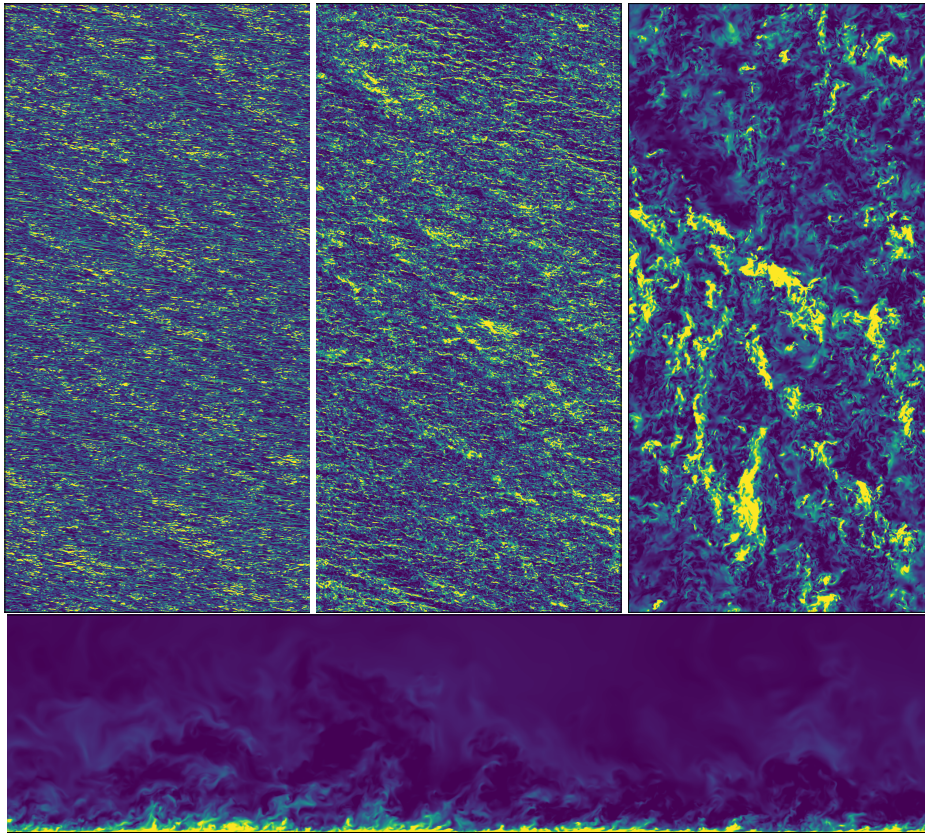


Fig. 3: horizontal slices of turbulence kinetic energy in the Buffer layer ( $i=10$ ), logarithmic Layer ( $i=100$ ), and outer layer ( $i=400$ ); coloring between percentiles 4 and 96 of the respective image. Lower panel:streamwise–vertical intersect through the domain

325 senting the scale separation or geometric size of the problem. This precludes, first,  
 326 a drag law wherewith we begin this section (4.1). Based on the scaling arguments  
 327 put forward in Sec. 3, we then develop, second, a formulation of the wind vector  
 328 in the Ekman layer (Sec 4.2). Finally, we come up with a separate formulation of  
 329 the, third, stream-wise and, fourth, span-wise velocity components in the overlap  
 330 and inner regions of the flow.

### 331 4.1 Drag-Law

332 A drag-law for Ekman flow determines—as a function of Reynolds number alone—  
 333 the surface drag. This can be formulated by the normalized surface friction,  $u_*$   
 334 (Eq. (1b), also termed geostrophic drag), and the direction of surface shear stress,  
 335  $\alpha_*$  (Eq. (1c), also termed wind veer). A non-zero veering of the wind is a rather  
 336 special case in comparison with most turbulent flows considered in an engineering

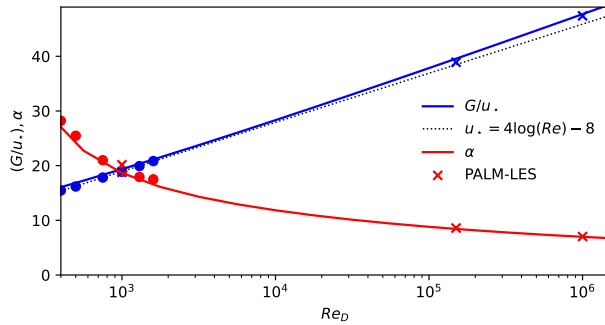


Fig. 4: Variation of geostrophic drag,  $Z_*$ , and surface veering,  $\alpha_*$ , with Reynolds number according to the theory by Spalart et al. (1989) and as estimated from DNS data

context, and it confronts us with a situation where the most appropriate coordinate system for analysis (namely that aligned with the surface shear stress) is a priori unknown. We compare our DNS data against a semi-empirical drag-law based on integral consideration (Spalart 1989) and find, as demonstrated in previous work (Ansorge and Mellado 2014), excellent agreement in the range  $400 < \text{Re} < 1600$ , representing a factor of 16 in variation of viscosity.

We also find that the solution of the transient equation involved in estimation of  $u_*$  for a given Reynolds number  $Re_D$  is approximated reasonably by the formulation

$$Z_* = 4 \log(\text{Re}_D) - 8 \quad (10)$$

which quantifies the 'weak' dependence of  $u_*$  on the Reynolds number as an approximately logarithmic one, at least for problems with a scale separation on the order that is relevant to geophysical problems ( $Re_D < 10^8$ ).

#### 4.2 Profile in the Ekman layer

Formulations for the outer layer that take into account the rotation (and thus deviation from the channel-flow analogy) need to be matched to the framework of surface similarity. A smooth transition from the inner layer to the Ekman layer, where the wind is characterized by a turning of its mean direction, is not easily achieved. Optis et al. (2014), for instance, define an "effective geostrophic wind vector that has the same magnitude of the observed surface geostrophic wind and is rotated by the angle  $\alpha$  [their nomenclature]" to overcome the unsteady transition when approaching the Ekman layer from below. Such rotation of the wind vector is *a posteriori* justified by the observational data that the model outcomes are compared to. This need for a connection of the two reference frames is a manifestation of a mismatch in the theoretical treatment of the inner and outer layer in this rotating flow configuration.

The text-book solution for Ekman flow makes use of the physical boundary conditions (BCs) for the ABL (no-slip at the bottom and geostrophic wind in the free atmosphere) and a constant eddy viscosity. Specifying the boundary conditions

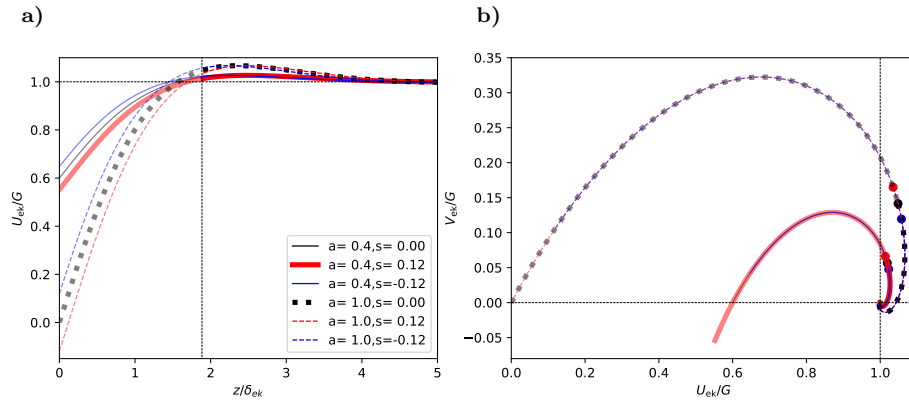


Fig. 5: **a)** Generalized Ekman-profile of the geostrophic-aligned component  $U_{ek}$ . **b)** Hodograph for the geostrophic-aligned and pressure-gradient aligned components  $U_{ek}$  and  $V_{ek}$ . Thick, black dashed line shows the classic solution. The height corresponding to  $z^- = 0.30$  is marked by the dashed line in panel (a) and by filled circles in panel (b). The hodograph and profiles above this reference height are shown as solid lines, below as opaque line.

365 at top and bottom eliminates one mode of the analytical solution, and it determines  
 366 the magnitude of the spiral. In doing so, one has to assume that the solution  
 367 is appropriate across the entire ABL, which is not the case: The dynamics put  
 368 forth by Ekman in 1905 are not appropriate in the surface layer of the ABL;  
 369 better approximations exist for the logarithmic, buffer, and viscous sublayers. In  
 370 view of this situation, we use an adapted Ekman spiral that does not enforce the  
 371 boundary conditions at the surface but at a different height. This is achieved by  
 372 considering the Ekman spiral only in the Ekman layer, thus giving way for the  
 373 well-established logarithmic and viscous-layer profiles in the lower surface layer.  
 374 Based on the derivation in App. A, this profile is given by

$$\frac{1}{G} \begin{pmatrix} U_{ek} \\ V_{ek} \end{pmatrix} = \begin{pmatrix} 1 \\ 0 \end{pmatrix} + e^{-z_{ek}} \left[ a_{ek} \begin{pmatrix} -\cos z_{ek} \\ \sin z_{ek} \end{pmatrix} + b_{ek} \begin{pmatrix} \sin z_{ek} \\ \cos z_{ek} \end{pmatrix} \right]. \quad (11a)$$

375 with  $z_{ek} = \delta_{ek}(y^- - s_{ek})$ . The right-hand-side consists of two modes with magni-  
 376 tude  $a_{ek}$  and  $b_{ek}$  shifted by  $\pi/2$  with respect to each other. In the classic case, the  
 377 second mode governed by  $b_{ek}$  is incompatible with the surface boundary condition.  
 378 While this is not the case here for the general form of the profile, the phase shifts  
 379 can also be captured by the parameter  $s_{ek}$ , and we stick with to a single-modal  
 380 approach, i.e., we let  $b_{ek} = 0$ .

381 This single-modal solution is characterized by three parameters, (i) an Ekman-  
 382 layer depth scale  $\delta_{ek}$ , (ii) the magnitude parameter of the spiral  $a_{ek}$ , and (iii) a  
 383 zero-crossing point for the velocity  $s_{ek}$ . The effects of varying these parameters  
 384 are illustrated in Fig. 5 where the classic Ekman solution is recovered by setting  
 385  $a_{ek} = 1$ ,  $s_{ek} = 0$  and  $\delta_{ek} = \sqrt{2\nu/f}$ . These parameters are *a priori* unknown as  
 386 they need to conform to the turbulent state of the boundary layer; we use our  
 387 DNS data to arrive at best estimates for them.

**The Ekman-layer depth scale**  $\delta_{\text{ek}}$  is fundamentally defined by the eddy viscosity. However, we have seen in Section 3 that a characteristic value for the eddy diffusivity is not easily obtained for its strong dependence on the Reynolds number and distance from the surface. We therefore resort to the physical manifestation of the eddy diffusivity in an Ekman layer, and use the boundary layer depth  $\delta_{\text{ek}} = 0.66\delta \times 2\pi$ . For the relation  $\delta_{\text{ek}} = \sqrt{2\nu_{\text{ek}}/f}$ , this yields  $\nu_{\text{ek}} \propto u_*^2/f$  in accordance with the observations in Sec. 3 (Eq. 9c).

**The magnitude parameter of the Ekman spiral**,  $a_{\text{ek}}$ , defines the super-geostrophic maximum of the wind profile aloft the logarithmic layer. Our simulations suggest this maximum of the velocity deficit remains constant when normalized by  $u_*$  as shown in Fig. 6. The numerical value of  $a_{\text{ek}}$  is estimated from visual comparison, and we find  $a_{\text{ek}} = 8.4u_*$ ; while this appears rather large, it is pre-multiplied by  $e^{-z_{\text{ek}}}$  which has already decreased to  $\mathcal{O}(0.1)$  at the height of this maximum. This choice ascertains that the velocity deficits  $U/u_* - Z_*$  and  $V/u_* - Z_*$  do not depend on the velocity scale  $u_*$ , but only on  $G$  as

$$U_{\text{ek}}/u_* - Z_* \propto a_{\text{ek}}Z_* = 8.4G. \quad (12)$$

Thus, the reduction of the area under the Ekman hodograph is directly linked to the variation in the friction velocity, which quantifies the well-known qualitative observation that a more turbulent boundary layer leads to a flatter hodograph in Ekman flow.

**The offset parameter**  $s_{\text{ek}}$  defines the zero-crossing height of the profile (in contrast to  $\delta_{\text{ek}}$ , which determines the thickness across which the wind veering takes place). Physically, this offset can be understood as the height at which the surface was located assuming a perfect Ekman flow down to the surface. As this is not the case, and gradients are steeper in the highly turbulent boundary layer flow encountered when approaching the surface, the offset is smaller than zero (the fully turbulent boundary layer is actually thinner than an Ekman layer would be). From our DNS data, we estimate  $s_{\text{ek}} = -0.12$ .

In summary, the outer layer of Ekman flow is characterized by a turning of the wind velocity and the super-geostrophic maximum that is sustained by momentum convergence at the inflection point of the velocity profile. The super-geostrophic maximum of streamwise velocity and a secondary minimum aloft the bulk-turbulent part of the boundary layer are well-described by a classic Ekman spiral with adapted boundary conditions and a shift in reference height. Corresponding profiles are shown in comparison with data from three DNS runs in Fig. 6. The idealized profiles capture the secondary minimum and convergence to the geostrophic equilibrium in the non-turbulent flow very well.

#### 4.3 Streamwise Velocity Component

For the streamwise velocity profile (that in non-rotating flows due to the geometry is always aligned with the surface shear stress), well-established theories exist for various regimes according to their distance from the wall and the relative role of viscosity, turbulence and interaction with the outer region of the flow with the logarithmic law for the mean velocity as a central anchor point.

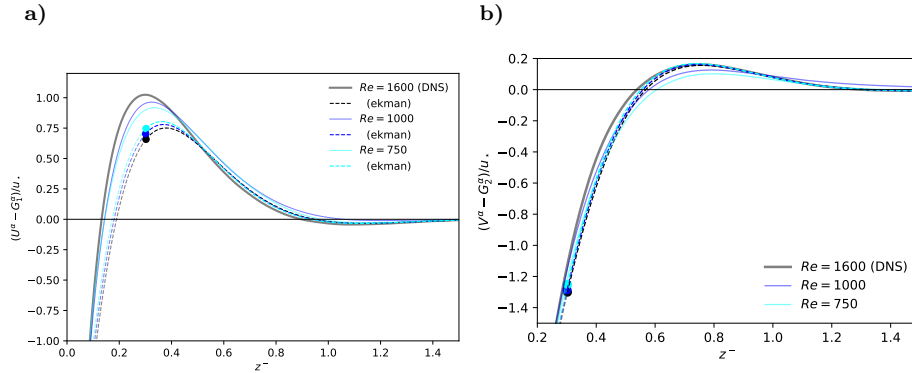


Fig. 6: Shear-aligned velocity deficit for the wall-streamwise (panel (a)) and wall-spanwise (panel (b)) components of the mean velocity  $U^\alpha$  and  $V^\alpha$ . Solid lines show DNS data, dashed lines the Ekman profiles  $U_{\text{ek}}$  and  $V_{\text{ek}}$  as defined in Eq. 11. Region below  $z^- = 0.3$  is shown opaque. Variations in  $U_{\text{ek}}$  and  $V_{\text{ek}}$  are a consequence of the normalization and related to changes in  $u_*$  and  $\alpha_*$  among the different  $Re_D$ .

430 In immediate vicinity to the surface, local turbulent mixing cannot occur for  
 431 the no-slip/no-penetration boundary condition, and the mean velocity is described  
 432 by a viscous profile of the form

$$U^{\alpha_*+} = z^+ \quad (13a)$$

433 where the direction of the velocity points into the exact opposite direction of the  
 434 wall shear stress  $\tau$ . In absence of roughness elements and for small roughness  
 435 ( $z_0^+ < 5$ ), this linear regime is known as viscous sub-layer Foken (2002); Foken  
 436 et al. (1978). In fact, this law of the wall has no degree of freedom given the  
 437 drag, i.e. once  $u_*$  and  $\alpha_*$  are defined. However, theoretical foundation is lacking  
 438 for the exact shape of the velocity profile in the buffer layer; though crucial for  
 439 turbulence production, it is commonly understood as a transition region between  
 440 the linear profile at the surface and the logarithmic profile aloft. A pure blending  
 441 from the linear velocity profile into the logarithmic one is, however, not reasonable  
 442 as both the linear and logarithmic profile overestimate the velocity in the buffer  
 443 layer. We therefore introduce a two-step correction procedure, accounting for the  
 444 smaller-than linear growth beyond  $y^+ \approx 5$ , and assuring smooth matching with  
 445 the logarithmic law at  $y^+ = 40$ :

$$U_{\text{inner}}^{\alpha_*+} = \frac{z^+}{1 + c_1(y^+)^2} + (c_2y^+ - a_{\text{match}}) \frac{1 + \tanh[0.2(y^+ - 22)]}{2} + c_3 e^{-c_4(y^+ - 22)^2}. \quad (13b)$$

446 We use here

$$c_1 = 0.00185; \quad c_2 = 0.195; \quad c_3 = 0.4; \quad c_4 = 0.35.$$

447 The second and third terms on the right hand side vanish for  $y^+ \ll 22$ , and  
 448  $c_1 = 0.00185$  implies an approximately 5% correction at  $y^+ = 5$  and an 18.5%  
 449 correction at  $y^+ = 10$ . The second and third term on the R.H.S. of eq. (13b) are  
 450 an empirical fit to the velocity profiles observed in the buffer layer and appear

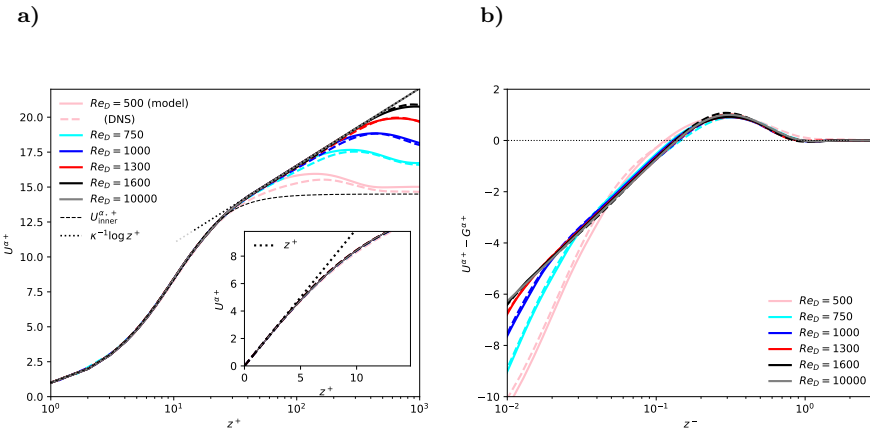


Fig. 7: Shear-aligned profiles of velocity components  $U^{\alpha*+}$  in inner (left) and outer (right) units.

451 independent of the Reynolds number for the range observed here. The coefficient  
 452  $a_{\text{match}}$ , which has no effect in the viscous sublayer, is then used to match this  
 453 formulation to the logarithmic law employed above.

454 In the logarithmic region, we use the profile

$$U_{\log}^{\alpha*+} = \frac{1}{\kappa} \log y^+ + C \quad (13c)$$

455 with the von-Kármán constant  $\kappa = 0.416$  and the boundary condition  $C = 5.4605$ .  
 456 For this logarithmic law,  $a_{\text{match}} = 3.569861$  for a matching at  $y^+ = 40$ .

#### 457 4.4 Spanwise velocity component

458 The background rotation and associated veering of the surface wind implies a  
 459 non-zero profile for the span-wise velocity which challenges the conventional as-  
 460 sumptions related to the channel-flow analogy: While the analogy with channel  
 461 flow in vicinity of the wall implies that the streamwise component be zero or at  
 462 least small, the veering requires a value of  $V_{top} = U_G \sin \alpha_*$  in the free stream (and  
 463 thus also at the top of the boundary layer if we assume that any substantial veloc-  
 464 ity gradient is confined to the turbulent part of the flow). This continuous rotation  
 465 of the wind vector is conveniently visualized by velocity hodographs aligned with  
 466 the outer, geostrophic flow (cf. Fig. 5b) and normalized by the geostrophic wind.  
 467 The geometry of the flow and its drag imply the following for any hodograph: (i)  
 468 the boundary conditions at the surface, (ii) the boundary condition at the top,  
 469 and (iii) the inclination of the hodograph at the origin by the surface veering:

$$V^{\alpha*}(z = 0) = 0, \quad (14a)$$

$$\lim_{z \rightarrow \infty} V^{\alpha*} = G \sin \alpha_* \quad (14b)$$

$$\partial_{z+} V^{\alpha*+} \Big|_{z=0} = 0. \quad (14c)$$

Outer scaling of the velocity profile further implies that the velocity deficit of  $(V^{\alpha_*} - G^{\alpha_*})/u_*$  be a universal function of the outer height  $z^-$ . In the outer region of the flow (for  $z^- \mapsto 1$ ),  $f_V(z^-)$ , should govern the spanwise velocity profile, as is supported by our DNS data (Fig.1b); above  $z^- \approx 0.3$ , this profile is very well approximated by the Ekman-turning derived above (Eq. (11); Fig. 6b). While this deficit is a signature of outer rotation, it is inappropriate to extend this general relation to the surface where inner scales matter: On the one hand, the variation of the spanwise velocity deficit across the boundary layer (i.e. between  $0 < z^- < 1$ ) must match the difference implied by the drag law ( $u_*, \alpha_*$ ) and the constant value of  $V^{\alpha_*}$  around  $z^- = 0.3$ . On the other hand, provided the outer velocity deficit is Re independent—the Re-dependence of  $\alpha_*$  and  $u_*$  implies that this difference cannot be constant as a function of Re

We hence ask, how does the span-wise component scale when the surface is approached? Clearly, the spanwise contribution is small in comparison with the streamwise component throughout much of the layer below  $z^- \approx 0.3$ . However, we cannot assume  $V = 0$  if a smooth matching between the inner and outer layers shall be achieved. In this context, we first realize that the velocity deficit  $(V^{\alpha_*} - G^{\alpha_*})/u_*$  approaches a Re-independent constant around  $C_{V0} = Z_* \sin \alpha = 6.1$  at the surface; deviations from this constant are only found for the lowest Reynolds numbers which is in accordance with the low-Re correction suggested by Spalart (1989). This constrains the wind veer, and it quantitatively shows that the decreasing wall friction manifest in an increase of  $Z_*$  exactly compensates the decrease of wind turning measured by  $\sin \alpha_*$ .

If the difference across the boundary layer is constant ( $C_{V0}$ ) vs. Re, the averaged gradient  $\partial_{z^+} V^{\alpha_* +}$  of the spanwise velocity component must decrease as  $1/\delta^+$  with increasing  $Re_\tau$ . Hence, it should—at a fixed height—be  $V^{\alpha_*} \propto (\delta^+)^{-1}$ . A profile that agrees with the constraints of the profile at the surface and exploits the dependence of  $V^{\alpha_*}$  on  $\delta^+$  is

$$V^{\alpha_*} \frac{\delta^+}{G} = f_{V,\text{visc}}(z^+) = v_{\text{ref}} \left( \omega_v z^+ - 1 + \exp[-\omega_v z^+] \right), \quad (15)$$

where  $v_{\text{ref}}$  controls the magnitude of the profile and  $\omega_v$  sets the height at which the profile transitions into an approximately linear one. We find excellent agreement with the DNS data for  $500 \leq Re_D \leq 1600$  below  $z^+ \approx 15$  with

$$v_{\text{ref}} = 18.85; \quad \omega_v = 0.2353$$

(cf. Fig. 8b).

For the adjacent surface layer, we find a log-like transition from the quasi-linear profile inner profile around  $z^+ = 10$  to a linear profile with increasing Re (Fig. 8b). We model this transition by

$$f_{V,\log}(z^+) = \frac{V_{\log}(z^+)}{G} \delta^+ = a_{\log} + b_{\log} \log z^+ + c_{\log} z^+. \quad (16)$$

This surface-layer profile matches the inner (viscous) scaling in vicinity of the surface to the outer (Ekman) scaling above  $z^- = 0.3$  when constrained by the

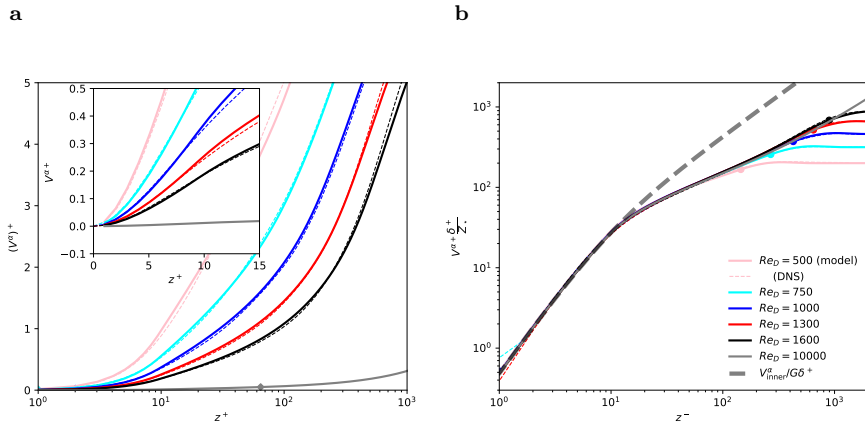


Fig. 8: Profiles of shear-aligned span-wise velocity  $(W^\alpha)^+$  versus inner height. Dashed lines show DNS data, thick, opaque lines are from the semi-empirical theory developed above. Left panel show standard inner normalization. Right panel shows the inviscid normalization yielding a universal profile for the spanwise component of velocity in the inner layer.

507 viscous profile at the bottom and the Ekman profile at the top:

$$f_{V,\log}(z^+ = 10) = \quad f_{V,\text{visc}}(z^+ = 10) =: \quad v_{10} \simeq 27.3 \quad (17)$$

$$\frac{\partial}{\partial z^+} [f_{V,\log}]_{z^+ = 10} = \quad \frac{\partial}{\partial z^+} [f_{V,\text{visc}}]_{z^+ = 10} =: \quad d_{10} \simeq 4.01 \quad (18)$$

$$f_{V,\log}(z^+ = 0.3\delta^+) = \quad V_{\text{ek}}^{\alpha*}(z^- = 0.3)\delta^+ =: \quad v_{03} \quad (19)$$

508 where  $v_{03}$  is determined by  $V_{\text{ek}}(0.3)$  and  $U_{\text{ek}}(0.3)$  and depends on  $\text{Re}$ . Given the  
 509 Ekman formulation of the velocity profile introduced in Sec. 4.2, one may express  
 510  $v_{03}$  using the Ekman profile introduced in Sec. 4.2 together with the approximation  
 511 for  $u_*(\text{Re})$  found in Eq. (10). While the  $\text{Re}$ -dependency of  $a_{\log}$ ,  $b_{\log}$ ,  $c_{\log}$  is small,  
 512 it shows up in Fig. 1 where the normalized profiles of spanwise velocity become  
 513 more convex with increasing  $\text{Re}$ . We can now quantify this effect by means of the  
 514 change of  $c_{\log}$  versus  $\text{Re}$  which is shown in Fig. 9 (cf. Appendix B;  $a_{\log}$  and  $b_{\log}$   
 515 are then determined by the universal values of  $v_{10}$  and  $d_{10}$ ).

## 516 5 Discussion

### 517 5.1 Implications for surface-layer scaling

518 Eq. (15) establishes a universal mixed scaling for the spanwise velocity in the vis-  
 519 ous layer: While it requires the vertical coordinate to be expressed in inner units,  
 520 the velocity itself is normalized by the geostrophic wind, and becomes inversely  
 521 proportional to the friction Reynolds number  $\text{Re}_\tau = \delta^+$  when considered at a fixed  
 522 height. In vicinity of the surface, such mixed scaling has already been identified  
 523 for higher-order statistics in convective flows (Mellado et al. 2016; Li et al. 2018),  
 524 where large scales leave their signatures in vicinity of the surface. It is important

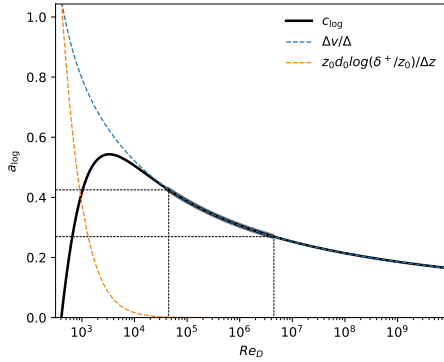


Fig. 9: Coefficients  $a_{\log}$ ,  $b_{\log}$  and  $c_{\log}$  (cf. Eq. 16) as a function of the viscous Reynolds number  $Re_D$ . The approximate range of scale separation relevant for atmospheric application is found in between the dotted lines, where  $a_{\log} \simeq 0$  and  $c_{\log} \simeq 0.4$

525 to note here that, while  $V$  is a first-order statistic from a statistical perspective,  
 526 the spanwise velocity is a higher-order correction term from the perspective of sim-  
 527 ilarity theory and from the viewpoint of the channel-flow analogy that is routinely  
 528 employed in the surface layer. Further, this is consistent with the scaling for the  
 529 velocity hodograph found in Eq. (12) where the friction velocity also drops out.

530 In the surface layer, there is not only a mixed scaling—as we had already iden-  
 531 tified in the viscous layer—but we cannot find a universal function onto which the  
 532 profiles of spanwise velocity collapse. This additional degree of freedom reflects the  
 533 inner–outer matching problem for the spanwise velocity, and rather than giving a  
 534 universal profile for this region, as is usually done, we resort here to a parametric  
 535 description of the problem, namely in terms of the function  $f_{V,\log}$  determined by  
 536 the parameters  $a_{\log}$ ,  $b_{\log}$ ,  $c_{\log}$  which can be estimated based on the above scaling  
 537 considerations for any Reynolds number. We note that, once the parameter  $a_{\log}$   
 538 is known, the parameters  $b_{\log}$  and  $c_{\log}$  can be estimated solely based on  $f_{V,\log}$ ,  
 539 i.e. using the value  $v_{10}$  and  $d_{10}$  found for the viscous region of the flow. For the  
 540 range of Reynolds number relevant to geophysical problems ( $10^4 \lesssim Re_D \lesssim 10^6$ ),  
 541 the variation of  $c_{\log}$  is, however, rather small.

## 542 5.2 Comparison with other theories

543 An alternative approach that considers viscous effects close to the surface is the  
 544 van-Driest scaling (Van Driest 1956), where an exponential damping of Prandtl's  
 545 mixing length is considered near the wall to yield

$$\frac{\partial u^+}{\partial y^+} = \frac{2}{1 + \sqrt{1 + (2\kappa y^+)^2 (1 - \exp[-y^+])}}; \quad (20)$$

546 the spanwise component is zero as no rotational effects are considered. Compar-  
 547 ing our proposed formulation for the stream-wise velocity in the inner layer to

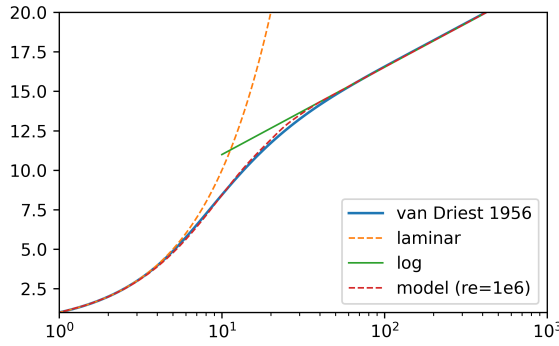


Fig. 10: Near-wall velocity profile according to the van-Driest scaling (blue, solid) in comparison with the present model (red, dashed), the viscous law of the wall (orange dashed), and the logarithmic law (green, solid)

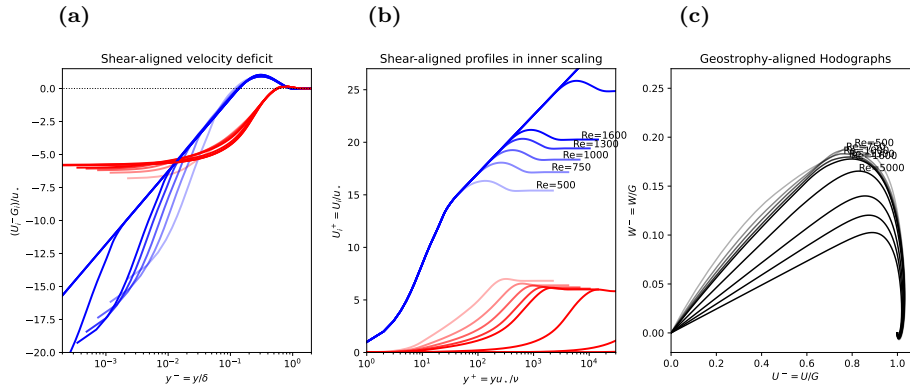


Fig. 11: (a) Velocity deficit, (b) velocity profile in shear-aligned hodographs and (c) hodograph in geostrophy-aligned coordinates. Thick, solid lines show theory, dashed lines data from DNS.

548 Van Driest's formulation yields later convergence of the velocity onto the logarithmic profile while, over all, it serves as an excellent model of the streamwise  
549 velocity component: Notable deviations (on the order of few percent) only occur  
550 in the region  $10 < z^+ < 30$ , where the velocity transitions from the linear to the  
551 logarithmic profile.

553 **Compare** to Emeis (2002) and Gryning (2007); highlight explicit knowledge  
554 on veering-profile  $\rightarrow$  directional sheer;

555 **Remember** of interpretation in the context of eddy viscosity (Fig. 2) Consider  
556 Townsend "Turbulent Shear Flow" Chapter 7.18: p. 319

557 Implications for **K-theory** (we now can consider that shear and stress are not  
558 necessarily perfectly aligned).  $\rightarrow$  can we do something to infer a K-profile from  
559 these theoretical considerations?

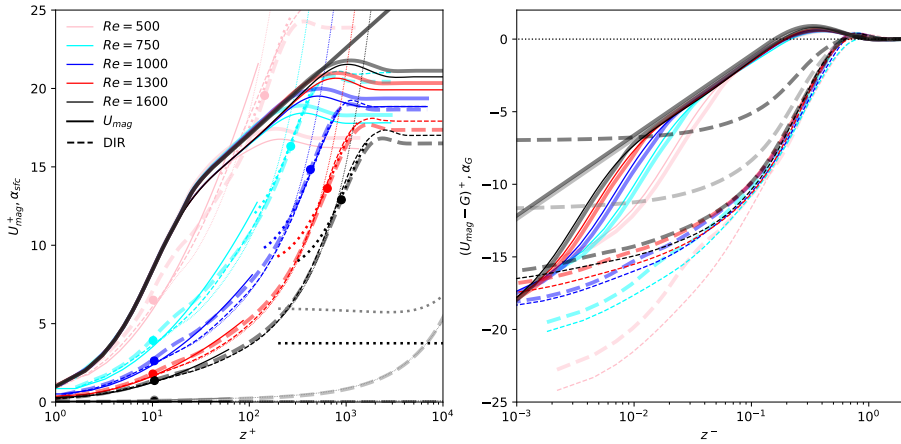


Fig. 12: Total velocity and veering (in degrees) vs inner and outer height. Dashed lines show DNS data, thick lines are from semi-empirical theory.

## 560 6 Conclusions

561 Applications:

- 562 – reference-shear for neutral profile approaches(systematic!) → wind engineering!
- 563 – initial condition for LES/DNS to eliminate/minimize inertial oscillation in
- 564 Benchmark simulations
- 565 –

## 566 References

- 567 Ansorge C (2019) Scale Dependence of Atmosphere–Surface Coupling Through  
568 Similarity Theory. *Boundary-Layer Meteorol* 170(1):1–27, DOI 10.1007/  
569 s10546-018-0386-y
- 570 Ansorge C (2024a) Direct numerical simulation of turbulent Ekman flow  
( $Re=0500$ ): DOI 10.17169/refubium-42505. DOI 10.17169/refubium-42505
- 572 Ansorge C (2024b) Direct numerical simulation of turbulent Ekman flow  
( $Re=1000$ ): DOI 10.17169/refubium-42507. DOI 10.17169/refubium-42507
- 574 Ansorge C (2024c) Direct numerical simulation of turbulent Ekman flow  
( $Re=1300$ ): DOI 10.17169/refubium-42508. DOI 10.17169/refubium-42508
- 576 Ansorge C (2024d) Direct numerical simulation of turbulent Ekman flow  
( $Re=1600$ ): DOI 10.17169/refubium-42509. DOI 10.17169/refubium-42509
- 578 Ansorge C, Mellado JP (2014) Global Intermittency and Collapsing Turbulence in  
579 the Stratified Planetary Boundary Layer. *Boundary-Layer Meteorol* 153(1):89–  
580 116, DOI 10.1007/s10546-014-9941-3
- 581 Ansorge C, Mellado JP (2016) Analyses of external and global intermittency in  
582 the logarithmic layer of Ekman flow. *J Fluid Mech* 805:611–635, DOI 10.1017/  
583 jfm.2016.534

- 584 Baars WJ, Marusic I (2020) Data-driven decomposition of the streamwise turbu-  
585     lence kinetic energy in boundary layers. Part 2. Integrated energy and. J Fluid  
586     Mech 882:A26, DOI 10.1017/jfm.2019.835
- 587 Barenblatt GI (1993) Scaling laws for fully developed turbulent shear flows. Part  
588     1. Basic hypotheses and analysis. J Fluid Mech 248:513–520, DOI 10.1017/  
589     S0022112093000874
- 590 Barenblatt GI, Goldenfeld N (1995) Does fully developed turbulence exist?  
591     Reynolds number independence versus asymptotic covariance. Phys Fluids  
592     7(12):3078–3082, DOI 10/bw2sq5
- 593 Blackadar AK, Tennekes H (1968) Asymptotic Similarity in Neutral Barotropic  
594     Planetary Boundary Layers. Journal of the Atmospheric Sciences 25:1015–1020,  
595     DOI 10.1175/1520-0469(1968)025<1015:ASINBP>2.0.CO;2
- 596 Brown AR, Beljaars ACM, Hersbach H, Hollingsworth A, Miller M, Vasiljevic  
597     D (2005) Wind turning across the marine atmospheric boundary layer. Quar-  
598     terly Journal of the Royal Meteorological Society 131(607):1233–1250, DOI  
599     10/dw2bxz
- 600 Calaf M, Meneveau C, Meyers J (2010) Large eddy simulation study of fully de-  
601     veloped wind-turbine array boundary layers. Phys Fluids 22(1):015,110, DOI  
602     10/b7gc6v
- 603 Coleman GN, Ferziger JH, Spalart PR (1992) Direct Simulation of the Stably  
604     Stratified Turbulent Ekman Layer. Journal of Fluid Mechanics 244:677–712,  
605     DOI 10.1017/S0022112092003264
- 606 da Silva CB, Hunt JC, Eames I, Westerweel J (2014) Interfacial Layers Between  
607     Regions of Different Turbulence Intensity. Annu Rev Fluid Mech 46(1):567–590,  
608     DOI 10.1146/annurev-fluid-010313-141357
- 609 Dimotakis PE (2005) TURBULENT MIXING. Annual Review of Fluid Mechanics  
610     37(1):329–356, DOI 10.1146/annurev.fluid.36.050802.122015
- 611 Ekman VW (1905) On the influence of the earth's rotation on ocean currents. Ark  
612     Mat Astron Fys, Vol 2 (1905), pp 1-53 2:1–53
- 613 Ellison TH (1955) The Ekman spiral. Q J Roy Met Soc 81(350):637–638, DOI  
614     10.1002/qj.49708135025
- 615 Emeis S (2018) Wind Energy Meteorology, 2nd edn. Atmospheric Physics for Wind  
616     Power Generation, Springer, Heidelberg
- 617 Emeis S, Baumann-Stanzer K, Piringer M, Kallistratova M, Kouznetsov R,  
618     Yushkov V (2007) Wind and turbulence in the urban boundary layer analysis  
619     from acoustic remote sensing data and fit to analytical relations. metz 16(4):393–  
620     406, DOI 10.1127/0941-2948/2007/0217
- 621 Esau I (2004) Simulation of Ekman Boundary Layers by Large Eddy Model with  
622     Dynamic Mixed Subfilter Closure. Environmental Fluid Mechanics 4(3):273–  
623     303, DOI 10/b8f3kh
- 624 Etling D (2002) Theoretische Meteorologie, 2nd edn. Eine Einführung, Springer-  
625     Verlag, Berlin, Heidelberg
- 626 Foken T (2002) Some aspects of the viscous sublayer. metz 11(4):267–272, DOI  
627     10.1127/0941-2948/2002/0011-0267
- 628 Foken Th, Kitajgorodskij SA, Kuznecov OA (1978) On the dynamics of the  
629     molecular temperature boundary layer above the sea. Boundary-Layer Mete-  
630     orol 15(3):289–300, DOI 10.1007/BF02652602
- 631 Ghannam K, Bou-Zeid E (2021) Baroclinicity and directional shear explain depar-  
632     tures from the logarithmic wind profile. Quarterly Journal of the Royal Meteo-

- 633      rological Society 147:434–464, DOI 10/gnj6z2
- 634      Gryning SE, Batchvarova E, Brümmer B, Jørgensen H, Larsen S (2007) On  
635      the extension of the wind profile over homogeneous terrain beyond the sur-  
636      face boundary layer. *Boundary-Layer Meteorol* 124(2):251–268, DOI 10.1007/  
637      s10546-007-9166-9
- 638      Höglström U (1988) Non-dimensional wind and temperature profiles in the atmo-  
639      spheric surface layer: A re-evaluation. *Boundary-Layer Meteorology* 42:55–78,  
640      DOI 10.1007/BF00119875
- 641      Höglström U (1996) Review of some basic characteristics of the atmospheric surface  
642      layer. *Boundary-Layer Meteorology* 78(3-4):215–246, DOI 10.1007/BF00120937
- 643      Jacobs AF, Van Boxel JH (1988) Changes of the displacement height and rough-  
644      ness length of maize during a growing season. *Agricultural Forest Meteorol*  
645      42(1):53–62, DOI 10.1016/0168-1923(88)90066-4
- 646      Jiang Q, Wang S, Sullivan P (2018) Large-Eddy Simulation Study of Log Laws  
647      in a Neutral Ekman Boundary Layer. *Journal of the Atmospheric Sciences*  
648      75(6):1873–1889, DOI 10.1175/JAS-D-17-0153.1
- 649      Kelly M, Gryning SE (2010) Long-Term Mean Wind Profiles Based on  
650      Similarity Theory. *Boundary-Layer Meteorol* 136(3):377–390, DOI 10.1007/  
651      s10546-010-9509-9
- 652      Kelly M, Troen I (2016) Probabilistic stability and ‘tall’ wind profiles: Theory  
653      and method for use in wind resource assessment. *Wind Energy* 19(2):227–241,  
654      DOI 10.1002/we.1829
- 655      Klein M, Maier RE, Schmidt H (2021) Stochastic modeling of transient neutral  
656      and stably-stratified Ekman boundary layers. *P A M M* 21(1):e202100,146, DOI  
657      10.1002/pamm.202100146
- 658      Li Q, Gentine P, Mellado JP, McColl KA (2018) Implications of Nonlocal Trans-  
659      port and Conditionally Averaged Statistics on Monin–Obukhov Similarity The-  
660      ory and Townsend’s Attached Eddy Hypothesis. *J Atmos Sci* 75(10):3403–3431,  
661      DOI 10.1175/JAS-D-17-0301.1
- 662      Lindvall J, Svensson G (2019) Wind turning in the atmospheric boundary layer  
663      over land. *Q J Roy Met Soc* 145(724):3074–3088, DOI 10.1002/qj.3605
- 664      Marusic I, Monty JP, Hultmark M, Smits AJ (2013) On the logarithmic region in  
665      wall turbulence. *J Fluid Mech* 716:R3, DOI 10.1017/jfm.2012.511
- 666      Mellado J, Ansorge C (2012) Factorization of the Fourier transform of the pressure-  
667      Poisson equation using finite differences in colocated grids. *Z angew Math Mech*  
668      92(5):380–392, DOI 10.1002/zamm.201100078
- 669      Mellado JP, van Heerwaarden CC, Garcia JR (2016) Near-Surface Effects of  
670      Free Atmosphere Stratification in Free Convection. *Boundary-Layer Meteorol*  
671      159(1):69–95, DOI 10.1007/s10546-015-0105-x
- 672      Mirocha JD, Churchfield MJ, Muñoz-Esparza D, Rai RK, Feng Y, Kosović B,  
673      Haupt SE, Brown B, Ennis BL, Draxl C, Sanz Rodrigo J, Shaw WJ, Berg LK,  
674      Moriarty PJ, Linn RR, Kotamarthi VR, Balakrishnan R, Cline JW, Robin-  
675      son MC, Ananthan S (2018) Large-eddy simulation sensitivities to variations of  
676      configuration and forcing parameters in canonical boundary-layer flows for wind  
677      energy applications. *Wind Energy Science* 3(2):589–613, DOI 10/gn3nh4
- 678      Moin P, Mahesh K (1998) Direct numerical simulation: A tool in turbulence re-  
679      search. *Annual Review of Fluid Mechanics* 30:539–578, DOI 10.1146/annurev.  
680      fluid.30.1.539

- 681 Momen M, Bou-Zeid E (2016) Large-Eddy Simulations and Damped-Oscillator  
 682 Models of the Unsteady Ekman Boundary Layer\*. *Journal of the Atmospheric*  
 683 *Sciences* 73(1):25–40, DOI 10.1175/JAS-D-15-0038.1
- 684 Momen M, Bou-Zeid E, Parlange MB, Giometto M (2018) Modulation of Mean  
 685 Wind and Turbulence in the Atmospheric Boundary Layer by Baroclinicity.  
 686 *Journal of the Atmospheric Sciences* 75(11):3797–3821, DOI 10/gfmn67
- 687 Monin AS (1970) The Atmospheric Boundary Layer. *Annual Review of Fluid*  
 688 *Mechanics* 2:225–250, DOI 10.1146/annurev.fl.02.010170.001301
- 689 Monin AS, Yaglom AM (1975) Statistical Fluid Mechanics, Vol. II, Dover Publi-  
 690 cations on Physics, vol II. Dover Publications, Inc., Mineola
- 691 Optis M, Monahan A, Bosveld FC (2014) Moving Beyond Monin-Obukhov Similar-  
 692 ity Theory in Modelling Wind-Speed Profiles in the Lower Atmospheric Bound-  
 693 ary Layer under Stable Stratification. *Boundary-Layer Meteorology* 153(3):497–  
 694 514, DOI 10.1007/s10546-014-9953-z
- 695 Rossby CG, Montgomery RB (1935) The layer of frictional influence in wind and  
 696 ocean currents. *Papers in Physical Oceanography and Meteorology* III(3):1–101
- 697 Sakagami Y, Haas R, Passos JC (2020) Generalized Non-dimensional Wind  
 698 and Temperature Gradients in the Surface Layer. *Boundary-Layer Meteorol*  
 699 175(3):441–451, DOI 10.1007/s10546-020-00510-3
- 700 Spalart PR (1989) Theoretical and numerical study of a three-dimensional turbu-  
 701 lent boundary layer. *J Fluid Mech* 205(-1):319, DOI 10.1017/S0022112089002053
- 702 Spalart PR, Coleman GN, Johnstone R (2008) Direct numerical simulation of the  
 703 Ekman layer: A step in Reynolds number, and cautious support for a log law  
 704 with a shifted origin. *Phys Fluids* 20(10):101,507, DOI 10.1063/1.3005858
- 705 Spalart PR, Coleman GN, Johnstone R (2009) Retraction: “Direct numerical sim-  
 706 ulation of the Ekman layer: A step in Reynolds number, and cautious support  
 707 for a log law with a shifted origin” [Phys. Fluids 20, 101507 (2008)]. *Phys Fluids*  
 708 21(10):109,901, DOI 10.1063/1.3247176
- 709 Stoll R, Gibbs JA, Salesky ST, Anderson W, Calaf M (2020) Large-Eddy Sim-  
 710 ulation of the Atmospheric Boundary Layer. *Boundary-Layer Meteorol* 177(2–  
 711 3):541–581, DOI 10/gmbmzw
- 712 Svensson G, Holtslag AAM (2009) Analysis of Model Results for the Turning  
 713 of the Wind and Related Momentum Fluxes in the Stable Boundary Layer.  
 714 *Boundary-Layer Meteorol* 132(2):261–277, DOI 10/bwknmt
- 715 Tennekes H (1973) A Model for the Dynamics of the Inversion Above a Convective  
 716 Boundary Layer. *Journal of the Atmospheric Sciences*
- 717 Van Driest ER (1956) On Turbulent Flow Near a Wall. *Journal of the Aeronautical*  
 718 *Sciences* 23(11):1007–1011, DOI 10.2514/8.3713
- 719 Zikanov O, Slinn DN, Dhanak MR (2003) Large-eddy simulations of the wind-  
 720 induced turbulent Ekman layer. *J Fluid Mech* 495:343–368, DOI 10/ccbpw

721 **A Laminar Ekman solution with consideration of inner layer**

$$\begin{pmatrix} \partial_t U \\ \partial_t W \end{pmatrix} = \begin{pmatrix} fW & + \nu \partial_z^2 U \\ -f(U - G) + \nu \partial_z^2 W \end{pmatrix} \quad (21a)$$

$$\Rightarrow \partial_t(U + iW) = f(W - i(U - G)) + \nu \partial_z^2(U + iW) \quad (21b)$$

722 In stationary conditions, this system is solved by

$$\hat{u}(z) = U_\infty + e^{-\gamma z} [A \cos \gamma z + B \sin \gamma z] \quad (21c)$$

$$\hat{w}(z) = W_\infty + e^{-\gamma z} [-A \sin \gamma z + B \cos \gamma z] \quad (21d)$$

723 where the constants  $U_\infty$ ,  $W_\infty$  set the top boundary condition and  $A$  and  $B$  set the bottom  
724 boundary condition. The most common boundary condition for a surface Ekman layer is  $A =$   
725  $U_\infty = G$ ,  $B = 0$ , and  $W_\infty = 0$ . The lower boundary condition, however, neglects the existence  
726 of the surface layer, and it appears reasonable to define  $A = cG$  where  $c < 1$  is a constant  
727 that incorporates the increased shear in the surface layer. Given a 'matching height'  $z_{match}$  and  
728 normalized matching height  $\xi = \gamma z_{match}$  in the upper part of the inner layer, we can match  
729 the Ekman profile to the inner layer by letting

$$\begin{aligned} u(z_{match}) &\equiv u_{match} = U_\infty + e^{-\xi} [A \cos \xi + B \sin \xi] \\ w(z_{match}) &\equiv w_{match} = W_\infty + e^{-\xi} [-A \sin \xi + B \cos \xi] \end{aligned} \quad (22)$$

$$\Rightarrow \begin{pmatrix} u_{match} - U_\infty \\ w_{match} - W_\infty \end{pmatrix} = e^{-\xi} \begin{pmatrix} A \\ B \end{pmatrix} \begin{pmatrix} \cos \xi & +\sin \xi \\ -\sin \xi & +\cos \xi \end{pmatrix} \quad (23)$$

(24)

731 Matching the profile at  $\xi = 0$ , one obtains  $A = \Delta u_{match}$  and  $B = -\Delta w_{match}$ ; and when the  
732 direction  $Ox$  is aligned with the geostrophic wind, we obtain the textbook-case  $A = |\mathbf{G}|$  and  
733  $B = 0$ .

734 Otherwise, choosing  $B \neq 0$  allows to introduce a phase shift of the Ekman rotation with  
735 respect to the decay of the wind spiral. As, however, in our context, the thickness and position  
736 of the spiral can already be controlled by the eddy viscosity and an offset in  $\zeta$ , here we let  
737  $B = 0$ .

## 738 B Matching the spanwise velocity profiles in the inner layer

739 The spanwise profile in vicinity of the surface is given by  $V/G = f_{V,visc} \delta^+$  with

$$f_{V,visc} = v_{ref} (\omega_v z^+ - 1 + e^{-\omega_v z^+}) \quad (25a)$$

$$f_{V,log} = a_{log} + b_{log} \log z^+ + c_{log} z^+ \quad (25b)$$

740 Matching the profiles and gradient  $z_0 = 10^+$  and the value at  $z_1 = 0.3\delta^+$  yields

$$v_{ref} (\omega_v z_0 + e^{-\omega_v z_0}) = v_0 = a_{log} + b_{log} \log z_0 + c_{log} z_0 \quad (26a)$$

$$v_1 = a_{log} + b_{log} \log z_1 + c_{log} z_1 \quad (26b)$$

$$v_{ref} \omega_z (1 - e^{-\omega_z z_0}) = d_0 = \frac{b_{log}}{z_{10}} + c_{log} \quad (26c)$$

741 The gradient condition implies  $b_{log} = (d_0 - c_{log}) z_0$ , and yields

$$v_0 - z_0 d_0 \log z_0 = a_{log} + c_{log} (z_0 - z_0 \log z_0) \quad (27a)$$

$$v_1 - z_0 d_0 \log z_1 = a_{log} + c_{log} (z_1 - z_0 \log z_0) \quad (27b)$$

$$\Rightarrow c_{log} = \frac{\Delta v - z_0 d_0 \log z_1 / z_0}{\Delta z} \quad (27c)$$

742 with  $\Delta z = z_1 - z_0$  and  $\Delta v = v_1 - v_0$ . Then, the coefficient  $a_{log}$  is estimated as

$$a_{log} = v_0 - z_0 d_0 \log z_0 - \frac{\Delta v - z_0 d_0 \log z_1 / z_0}{\Delta z} [z_0 - z_0 \log z_0]. \quad (27d)$$

743 We note that  $\log(z_1/z_0)/(z_1 - z_0) \rightarrow 0$  for large  $z_1$ , and as  $z_1 = 0.3\delta^+$ , this implies that the  
744 second term in  $c_{log}$  only plays a role at low and intermediate Re. Then,  $a_{log}$  can be estimated  
745 as

$$a_{log} \simeq v_0 - z_0 \left[ d_0 \log z_0 - \frac{\Delta v}{\Delta z} (1 - \log z_0) \right] \quad (27e)$$

746 for large Re.

---

**A Old Stuff**

[OLD FROM HERE] Below this region, the gradients in span-wise velocity are rather small and the span-wise velocity monotonically approaches its surface boundary condition  $V(z = 0) = 0$ . While the streamwise velocity follows a universal inner scaling that has acquired its universal,  $Re$ -independent shape for  $Re_D > \mathcal{O}(10^3)$ , the span-wise component that defines how the velocity vector veers when the surface is approached, does not collapse in inner units, and there is, most importantly no sign of convergence even at the highest Reynolds numbers for which simulations were carried out. Even though the simplest assumption  $V = 0$  is reasonable for the lower part of the surface surface layer ( $z^- < 10^{-3}$ ), it does not appropriately capture the profile in the rest of the surface layer:

First,  $V = 0$  implies a discontinuity in the velocity profile at  $z^- = 0.1$ , where the outer scaling found above yields a finite value at geophysical  $Re$ , i.e. there is non-zero veering in the upper part of the surface layer—as is well-known also from field observation. Second, the layer around  $z^- = 0.1$  is crucial to obtain the characteristic and well-established shape of the hodographs as the layer where  $V$  sets in marks the ‘maximum’ of  $V^-$  vs.  $U^-$ .

The scale for the magnitude of the span-wise velocity component is  $u_* \sin \alpha$ . Based on our DNS data, we suggest that the Reynolds number scaling of this velocity-magnitude scale is captured by  $Re_\tau^{-1/2}$  which is indeed known from the generalization of higher-order statistics, such as turbulent fluxes in the inner layer (Marusic et al. 2013) that also follow a mixed scaling in the inner layer. We then parameterize the spanwise velocity at 10 wall units as anchor point in the inner layer:

$$V_{10} \equiv V(z^+ = 10) = 750 \frac{u_* \sin \alpha}{\sqrt{Re_\tau}}. \quad (28a)$$

This leaves us with three fixed points of the velocity profile in the inner layer, namely (i) the boundary condition  $V_0 = 0$ , (ii)  $V_{10}$  at  $z^+ = 10$ , and (iii) the lower end of the logarithmic profile at  $z^- = 0.1$  where the latter two are semi-empirically estimated from DNS data. In absence of well-established scaling considerations for the span-wise velocity, the choice of profile fits joining these three points is indeed arbitrary, but we can resort to the DNS data for an empirical approach and find that a square-root profile fits  $V(z^+)$  in the surface layer. A linear profile for  $V$  is employed in the viscous sub-layer. Based on the physical extent of the viscous sub-layer in Ekman flow around five wall units (Foken 2002; Ansorge 2019), we choose  $z^+ = 5$  to transition from one to the other and note that  $V$  is already very small at this height. The span-wise velocity profile in the surface layer is then estimated as

$$V(z^+) \Big|_{\text{inner}} = \begin{cases} a_1 z^+ & ; z^+ \leq 5 \\ b_1 + b_2 \sqrt{z^+} & ; 5 < z^+ < Re_\tau/10 \end{cases}, \quad (28b)$$

with  $b_1$  and  $b_2$  estimated such that

$$\begin{aligned} V(z^+ = 10) \Big|_{\text{inner}} &= V_{10} \\ V(z^+ = Re_\tau/10) \Big|_{\text{inner}} &= V_{\text{outer}}(0.1) \end{aligned} \Rightarrow \begin{cases} b_2 = \frac{V_{\text{outer}}(0.1) - V_{10}}{\sqrt{Re_\tau/10} - \sqrt{10}} \\ b_1 = V_{10} - \sqrt{10}b_2 \end{cases} \quad (28c)$$

We then estimate  $\alpha$  from the matching condition at  $z^+ = 5$ , i.e.

$$5a = b_1 + \sqrt{5}b_2 \Rightarrow a = \frac{1}{5} \left[ V_{10} + (\sqrt{5} - \sqrt{10}) \left( \frac{V_{\text{outer}} - V_{10}}{\sqrt{Re_\tau/10} - \sqrt{10}} \right) \right]. \quad (28d)$$

*Matching region.* While the profile composed of  $V_{\text{inner}}(z^+ \leq 0.1 Re_\tau)$ ,  $V_{\text{outer}}(z^- > 0.1)$  is continuous, it is not smooth at  $z^- = 0.1$ , i.e. at the transition from power-law ( $V \propto \sqrt{z^+}$ ) to logarithmic scaling. To alleviate this issue, we use a second-order polynomial for transition from the inner to the outer layer in the range  $z_{\text{low}} < z < z_{\text{up}}$  such that

$$V_{\text{trans}}(z^-) = V_{\text{inner}}(z_{\text{low}}^+) + \Delta V (az_{\text{arg}} + b(z_{\text{arg}})^2) \quad (28e)$$

784 with  $\Delta V = V_{\text{outer}}(z_{\text{up}}^-) - V_{\text{inner}}(z_{\text{low}}^+)$  and  $z_{\text{arg}} = (z - z_{\text{low}})/(z_{\text{up}} - z_{\text{low}})$ . It is  $a + b = 1$  for  
 785  $V_{\text{trans}}(z_{\text{up}}^-) = V_{\text{outer}}(z_{\text{up}}^-)$ , and we constrain  $a$  by

$$\frac{\partial V_{\text{trans}}}{\partial z^-} \Big|_{z=z_{\text{low}}} = \frac{\partial V_{\text{inner}}}{\partial z^-} \Big|_{z=z_{\text{low}}}, \quad (28f)$$

786 where we find that  $z_{\text{low}}^- = 0.06$  and  $z_{\text{up}}^- = 0.13$  yield satisfactory agreement with DNS data.